2010

# Mapping Circulation in the Kuroshio Extension with an Array of Current and Pressure Recording Inverted Echo Sounders

Kathleen A. Donohue
*University of Rhode Island*, kdonohue@uri.edu

D. Randolph Watts
*University of Rhode Island*, randywatts@uri.edu

Karen L. Tracey
*University of Rhode Island*, krltracey@uri.edu

Andrew D. Greene
*University of Rhode Island*

Maureen A. Kennelly
*University of Rhode Island*



## Citation/Publisher Attribution

Donohue, K.A., D.R. Watts, K.L. Tracey, A.D. Greene, and M. Kennelly, 2010: Mapping Circulation in the Kuroshio Extension with an Array of Current and Pressure Recording Inverted Echo Sounders. *J. Atmos. Oceanic Technol.*, **27**, 507–527, https://doi.org/10.1175/2009JTECHO686.1
Available at: https://doi.org/10.1175/2009JTECHO686.1

Mapping Circulation in the Kuroshio Extension with an Array of Current and Pressure Recording Inverted Echo Sounders

# Mapping Circulation in the Kuroshio Extension with an Array of Current and Pressure Recording Inverted Echo Sounders

KATHLEEN A. DONOHUE, D. RANDOLPH WATTS, KAREN L. TRACEY, ANDREW D. GREENE, AND MAUREEN KENNELLY

*Graduate School of Oceanography, University of Rhode Island, Narragansett, Rhode Island*

(Manuscript received 6 January 2009, in final form 11 September 2009)

ABSTRACT

The Kuroshio Extension System Study (KESS) aimed to quantify processes governing the variability of and the interaction between the Kuroshio Extension and the recirculation gyre. To meet this goal, a suite of instrumentation, including 43 inverted echo sounders equipped with bottom pressure gauges and current meters [current and pressure recording inverted echo sounders (CPIES)], was deployed. The array was centered on the first quasi-stationary meander crest and trough east of Japan, which is also the region of highest eddy kinetic energy. KESS was the first experiment to deploy a large quantity of these new CPIES instruments, and it was unique in that the instruments were deployed in water depths (5300–6400 m) close to their limit of operation. A comprehensive narrative of the methodology to produce mesoscale-resolving four-dimensional circulation fields of temperature, specific volume anomaly, and velocity from the KESS CPIES array is provided. In addition, an improved technique for removing pressure drift is introduced. Methodology and error estimates were verified with several independent datasets. Temperature error was lowest on the equatorward side of the Kuroshio Extension core and decreased with depth (1.5°C at 300 m, 0.3°C at 600 m, and <0.1°C below 1200 m). Velocity errors were highest in regions of strong eddy kinetic energy, within and south of the jet core. Near the surface, the error in geostrophic velocity between adjacent CPIES was typically 10 cm $s^{-1}$, decreasing downward to 6 cm $s^{-1}$ at 500-m depth and 5 cm $s^{-1}$ below 800 m. The rms differences from pointwise current measurements are nearly twice as large as the geostrophic errors, because the pointwise velocities include submesoscale and ageostrophic contributions.

## 1. Introduction

The Kuroshio Extension (KE) System Study (KESS) aimed to identify and quantify the processes governing the variability of and the interaction between the KE and the recirculation gyre. Specific goals included the determination and quantification of cross-frontal exchange, the interaction between upper and deep circulation, and the processes that govern the strength and structure of the recirculation gyre.

The KESS array comprised inverted echo sounders (IESs) equipped with bottom pressure gauges and current meters [current and pressure recording IESs (CPIES)] and a series of subsurface moorings deployed across the jet (Donohue et al. 2008). Each subsurface mooring was equipped with an upward-looking acoustic Doppler current profiler (ADCP) located near 200-m depth; a McLane moored profiler (MMP), which traveled between 250- and 1500-m depths; and several current meters below 1500 m. A surface buoy, the Kuroshio Extension Observatory (KEO) funded by the National Oceanic and Atmospheric Administration (NOAA), is part of the global network of OceanSITES (see http://www.oceansites.org/index.html) time series reference sites, and its measurements continue past the KESS field program as part of a joint United States–Japan collaboration. The KESS moored array, which was deployed in summer 2004 and recovered in summer 2006, was centered on the first quasi-stationary meander crest and trough east of Japan, which is also the region of highest eddy kinetic energy (Fig. 1). Field work also included the deployment of 40 Argo profiling floats, intensive synoptic hydrographic surveys, and atmospheric soundings.

Methods for interpreting the IES travel time measurements $\tau$ have evolved over the past 30 yr since the

*Corresponding author address:* Kathleen A. Donohue, Graduate School of Oceanography, University of Rhode Island, 215 South Ferry Road, Narragansett, RI 02882.
E-mail: kdonohue@gso.uri.edu

DOI: 10.1175/2009JTECHO686.1

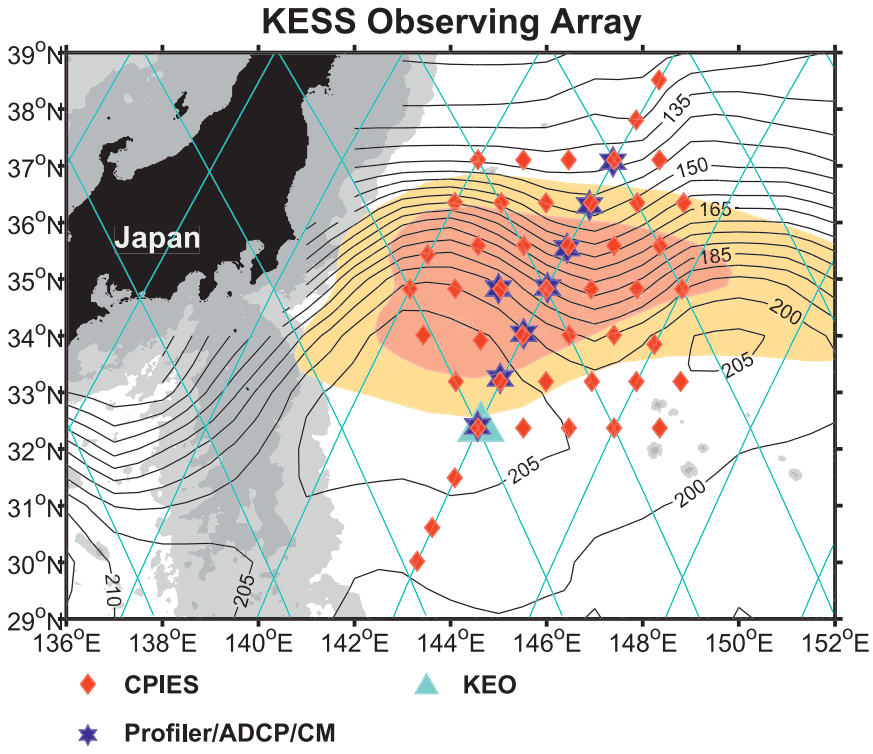


FIG. 1. The mesoscale in situ KESS instrument array was centered on the first quasi-stationary meander trough east of Japan and in the region of highest eddy kinetic energy. The array comprised PIES, CPIES (red diamonds), and McLane moored profilers (blue stars) equipped with upward-looking acoustic Doppler current meters and deep current meters. As part of the global network of OceanSITES, a surface buoy, KEO (blue triangle), was outfitted with sensors to measure air–sea fluxes and upper-ocean temperature and salinity. Solid contour lines are the GDEM mean surface dynamic height contours in dyn cm from Teague et al. (1990) referenced to 1000 dbar. The 2000- and 4000-m isobaths are shaded dark and light gray, respectively. Eddy kinetic energy determined from satellite sea surface height anomaly >0.18 and 0.24 $m^2$ $s^{-2}$ were color shaded yellow and orange, respectively.

instrument was developed (Rossby 1969) and subsequently deployed by Watts and Rossby (1977) during Mid-Ocean Dynamics Experiment (MODE). They established linear relationships between $\tau$ and integral quantities such as dynamic height and heat content. In early Gulf Stream studies, $\tau$ measurements were used to monitor thermocline depth variations to track the position of the front and determine meander characteristics (Watts and Johns 1982; Tracey and Watts 1986). When pressure sensors were added to the instrument package [pressure-sensor-equipped inverted echo sounders (PIES)], techniques to identify and remove pressure drifts were developed (Watts and Kontoyiannis 1990). Objective mapping was adapted to $\tau$ measurements from the Gulf Stream frontal region where nonhomogeneous statistics prevail (Watts et al. 1987), and these methods were further refined to include an iterative mapping scheme (Tracey et al. 1997). The work of He et al. (1998) determining geostrophic velocity shear profiles assuming a parallel isotherms model led to the development of the gravest empirical mode (GEM) lookup tables (Meinen and Watts 2000; Sun and Watts 2001; Watts et al. 2001b) that could be used in conjunction with measured $\tau$ to obtain full-water-column temperature and specific volume anomaly profiles. Using the combination of PIES and deep current meters, Watts et al. (2001a) leveled bottom pressure measurements to a common geopotential that could provide the deep velocity reference for geostrophic velocity profiles obtained via the GEM method (Fig. 2). Examination of dynamic height and travel time relationships in the North Atlantic by Trivers and Wimbush (1994) led Watts et al. (2001b) to use a constant value of gravity to determine $\tau$ when constructing their GEMs from hydrocasts that spanned a wide range of latitudes. Further developments by Watts et al. (2001b), Book et al. (2002), and Park et al. (2005) include a seasonal cycle in the lookup tables. The GEM method has been successfully used not only in the Gulf Stream (Meinen et al. 2009) but also in the North Atlantic Current (Meinen and

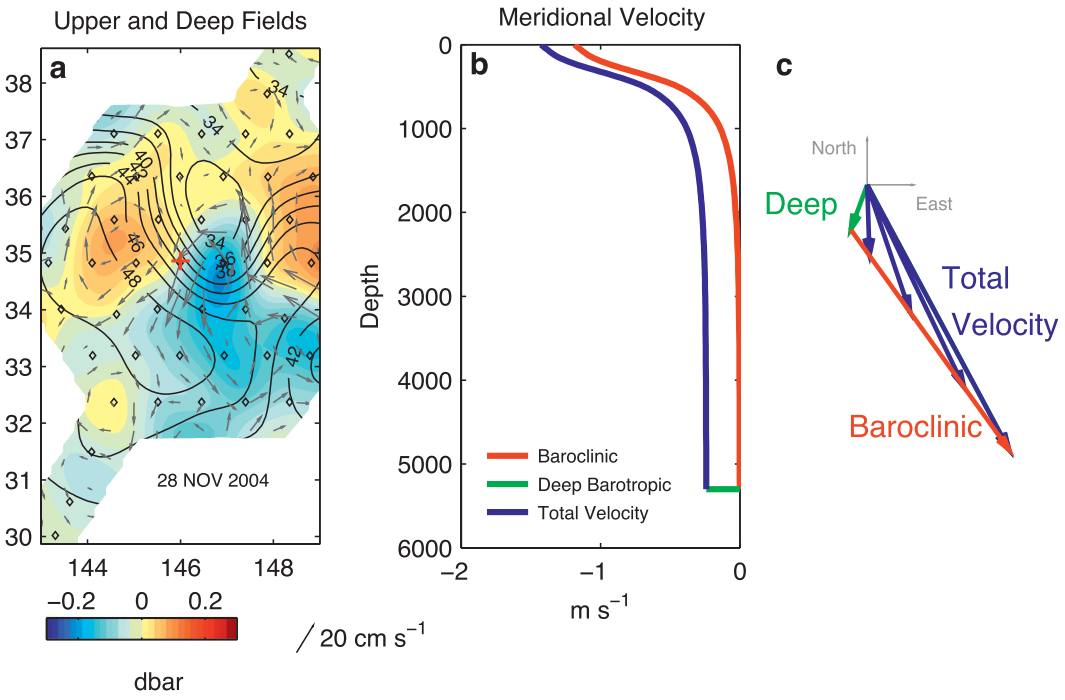


FIG. 2. With the CPIES array, current profiles were calculated as the sum of a baroclinic velocity referenced by a deep barotropic velocity. The subthermocline currents were observed to be nearly independent of depth, and operationally we defined barotropic as the reference velocity at 5300 dbar. (a) The upper baroclinic geopotential streamfunction shown with solid contours [contour interval (CI) = 2 $m^2 s^{-2}$]. Mapped barotropic pressure field is color shaded (CI = 0.02 dbar). Gray arrows indicate gridded deep barotropic currents (scale at bottom right). (b) Total velocity (blue) is calculated by referencing the baroclinic velocity profile (red) with the deep barotropic velocity (green). Profiles of the meridional component are illustrated for the mid-Kuroshio location shown in (a) (red cross), where cross-frontal geostrophic flow ≈30 cm $s^{-1}$ occurred between a deep anticyclone (orange hues) and cyclone (blue hues). (c) The vector sum of deep barotropic velocity (green arrow) and baroclinic velocity (red arrows with magnitude dependent on depth) produces the total velocity (blue vectors turning with depth). A baroclinic velocity profile that is vertically aligned like this is called equivalent barotropic.

Watts 2000), the Antarctic Circumpolar Current (Watts et al. 2001b), the Japan/East Sea (Park et al. 2005), the Gulf of Mexico Loop Current (Donohue et al. 2006), and the Kuroshio (Book et al. 2002). A comprehensive list of IES publications may be found at URI/GSO (2009).

Over the past few years, a new version of the IES has been developed at the University of Rhode Island. This latest model, called a CPIES, not only includes a Paroscientific pressure sensor but also an Aanderaa Doppler current sensor (RCM-11). The combined instrument package with its own acoustic release is more cost effective to deploy than separate PIES and current-meter moorings. The internal microprocessor allows the data to be processed in situ, making them suitable for retrieval by acoustic telemetry. Digital storage capacity and lithium battery packs enable deployment periods for up to five years. Recently, a line of six CPIES and acoustic Doppler current profilers measured the Kuroshio in the East China Sea (Andres et al. 2008). KESS was the first experiment to deploy a two-dimensional array of these new CPIES instruments, and it was unique in that the instruments were deployed in water depths (5300–6400 m) close to their limit of operation.

Because of these advances in instrumentation and data interpretation, the use of IESs by other investigators has become more widespread. To consolidate the description and rationale behind the various processing techniques, here we provide a comprehensive narrative of the methodology to produce mesoscale-resolving four-dimensional circulation fields of temperature, specific volume anomaly, and velocity from the KESS CPIES array. An improved technique to remove pressure drift is presented. Additionally, several independent datasets (profiling floats, current meters, and McLane moored-profiler measurements) validate the methodology and error estimates.

## 2. KESS experimental design

The design of the KESS array was based on the following considerations: First, the array was in the region of maximum eddy kinetic energy. Second, the 525-km

(32.4°–37.11°N) meridional extent of the main array would be sufficient to ensure that it almost always fully captured the meander envelope of the KE and extended meridionally into the adjacent waters. Third, the zonal width of the KESS CPIES array encompassed the typical meander wavelength. Fourth, the mesoscale resolution was sufficient to enable a study of dynamical balances. Based on analysis by Koblinsky et al. (1984), which indicated an isotropic spatial correlation length scale near 90–100 km for temperature at 300-m depth in the region, the nominal array spacing was chosen to be 88 km (sections 3 and 4 examine the correlation length scales from the KESS $\tau$ and pressure observations). Finally, as many instruments as possible were located along Jason ground tracks.

### a. Data return

In April through May 2004, KESS measurements began with the deployment of 43 CPIES and 3 PIES (Fig. 3) with the intent to leave the instruments undisturbed and sampling for a two-year duration. The tall moorings had current meters at 5000-m depth; therefore, we deployed three PIES at F3, D4, and B4 rather than duplicate deep current measurements at these sites.

In June–July 2005, the first year of data were acoustically telemetered. Two problems were discovered: battery passivation and water shorts in the current-meter cables resulting from leaks. KESS was the first time CPIES were deployed at ocean depths near the operating limit; the high pressures caused failures in cable terminations because of a manufacturing fault in that batch: 9 CPIES quit sampling because of passivation and 11 had leaky current-meter cables—2 of these stopped recording because of passivation. Most of these sites recorded data until March or July 2005. Five sites had duplicate instruments (C3, C5, E7, F3, and N1) as backups for acoustic command problems at the time of their deployments. The instruments at many sites were turned around, but some CPIES were replaced with PIES because of the current-meter cable failures (C2, C3, D2, E1, E4, and E7). Two sites on the array periphery (F1 and G6) were left empty during the second year. At midexperiment, the 44 occupied sites consisted of 35 CPIES and 9 PIES.

Recovery took place in June 2006: 48 PIES and CPIES were recovered from 44 sites. Ultimately, the problems with the acoustic command systems at the duplicate sites were resolved. All but one of the instruments, C2, were recovered. Fortunately, its records were retrieved by acoustic telemetry from the instrument on the seafloor to the ship. The instrument internally processed data in a manner similar to postprocessing techniques and saved daily values. The telemetered pressure data processing used a Godin filter to ensure that tides were not aliased. Although the Godin filter does not deterministically remove the tides, it reduces the eight principal tidal components in KESS to amplitudes less than 0.007 cm leakage of the diurnal components and 0.0004 cm leakage of the semidiurnal components.

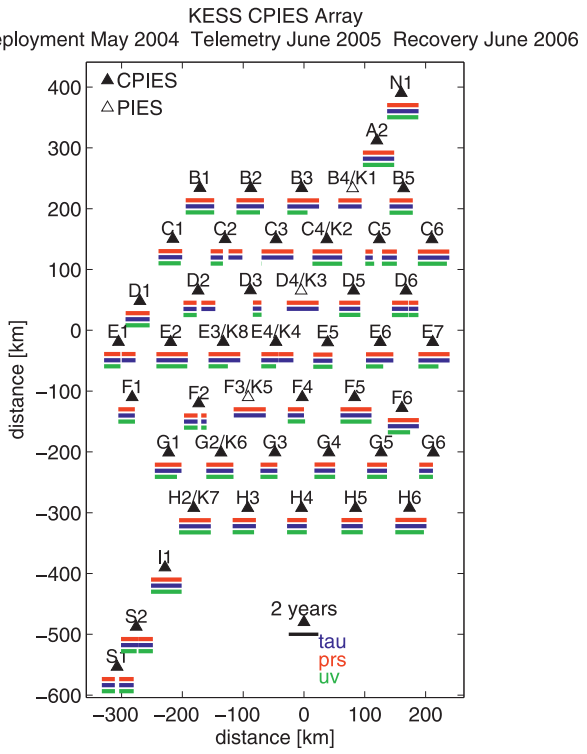


FIG. 3. KESS CPIES (filled triangles) and PIES (open triangles) sites. The timeline beneath each site indicates data return as a function of measurement: $\tau$ is blue, bottom pressure is red, and current is green. The key in the bottom-right corner provides the time scale. The profiler moorings K1–K7 coincided with CPIES and PIES sites along the diagonal between B4 and H2 during both years. An additional profiler, K8, was added at site E3 during the second year.

With the final KESS dataset, current and density were mapped for the entire region for 16 months through September 2005 and later for subregions through May 2006 as instruments failed. About 75% (55%) of the array area could still be mapped in January 2005 (April 2006). This paper focuses on the 16-month mapping period, and the error techniques described here would be applicable to subregions. Note that during this ''good mapping period'' the CPIES at site D3 did not record measurements during the first deployment. A complete and detailed report of the KESS time series processing may be found in Kennelly et al. (2008).

### b. Inverted echo sounder

The inverted echo sounder measures the vertical round-trip acoustic travel time of a 12.0 kHz pulse from sea floor to sea surface and back, $\tau$ (Watts and Rossby 1977). Each hour, the CPIES transmits 24 pings and the return times are recorded internally. The detector resolution was 0.03 ms (see URI/GSO 2009). The return echo has a Rayleigh-shaped distribution for a one-hour ensemble with standard deviation of 2.2 ms. To reduce this noise in the $\tau$ measurement, primarily because of scatter from sea surface roughness, the 24 values were processed through a two-stage windowing and median filtering, which yielded an hourly estimate (Kennelly et al. 2007). Each instrument's hourly time series was low-pass filtered with a fourth-order Butterworth filter with a cutoff period of 72 h, and the beginning and end of the records were truncated to remove transients. The filtered records were then subsampled at 12-h increments. The error in the hourly (and low-pass) $\tau$ measurement expressed as a standard error is (2.2 ms) $(24^{-1/2}) = 0.45$ ms [(2.2 ms) $(24 \times 72)^{-1/2} = 0.05$ ms].

### c. Pressure

The CPIES measured pressure every 10 min and an average of six 10-min measurements created an hourly estimate. The quartz pressure sensor made by Paroscientific has a stated accuracy of 0.01% of full scale (Houston and Paros 1998), which was approximately 0.6 dbar (1 dbar = 10 kPa) for the 10 000 psi sensors used in KESS. The resolution of these bottom pressure measurements was 0.1 mbar (URI/GSO 2009).

Tidal response analysis (Munk and Cartwright 1966) determined eight major tidal constituents for each instrument. The tidal range was about 1 m in the KESS region, and the estimated amplitudes and phases varied smoothly across the array. The amplitudes of the tidal constituents ranged from a high near 20 cm for M2 and K1 to near 16 cm for O1, 10 cm for S2, and less than 6 cm for the remaining semidiurnal constituents.

Experience indicates that preconditioning greatly reduces pressure drift (Watts and Kontoyiannis 1990). Sensors were subjected to pressures near 3000 dbar for 1–2 months in the laboratory prior to their deployment. Despite these precautions, most of the instruments exhibited some drift (less than 0.35 dbar at most sites). In section 3, we present a new and improved technique to estimate and remove the pressure drift. Briefly, the bottom current meters determined a time series of streamfunction at each CPIES site. Bottom pressure records are then required to match the current-meter-derived geostrophic mean pressure estimates. This methodology dedrifted and leveled the pressure records simultaneously. The advantage of this method is that it takes advantage of the deep velocity measurements to help distinguish ocean signals from instrumental drift.

Finally, each demeaned hourly pressure time series was low-pass filtered and subsampled in the same manner as the travel time records. The KESS array had three sites occupied by two instruments separated by less than 1 km. The 0.007-dbar error in the residual pressure, expressed as a standard deviation, was estimated by evaluating the difference between the three paired records over their overlapping time period.

### d. Current

The CPIES sampled currents every 20 min (two sites, S1 and S2, had 10-min sampling for the first year). Three corrections were applied to the data. First, a local magnetic declination was applied. Second, because the instruments utilized a nominal speed of sound of 1500 m $s^{-1}$, processing included a speed of sound correction appropriate for each instrument's depth (speed of sound at 5500-m depth in the KESS array is near 1550 m $s^{-1}$). Finally, Hogg and Frye (2007) showed that the RCM-11 speeds are biased low; speed was multiplied by a factor of 1.1. Speed and direction were then converted to zonal and meridional velocity and averaged hourly. Subsequently, the currents were low-pass filtered and subsampled to coincide with $\tau$ and pressure.

The difference between currents measured by the CPIES and the deepest tall mooring current meters (also RCM-11s) for the five instrument pairs provided an error of 1.37 cm $s^{-1}$. Some of these differences can be attributed to spatial differences, because the moorings were located more than 5 km from the CPIES and the current meters were shallower (5000-m depth). Uncertainty in the Hogg and Frye (2007) rescaling (1.1–1.15) contributes another 0.6 cm $s^{-1}$. In addition, we assigned an error of 0.08 cm $s^{-1}$ because of CPIES current-meter mooring motion. Altogether, we considered the deep current measurement error to be 1.5 cm $s^{-1}$ for the 72-h low-passed time series.

## 3. Mapping deep bottom pressure and current

The bottom pressure and velocity were jointly mapped using multivariate optimal interpolation constrained to be geostrophic with a Gaussian correlation function (Bretherton et al. 1976; Watts et al. 2001a). The KESS array including southern and northern antennae spanned almost 8.5° latitude; the range of the Coriolis parameter through the array was 22% of its array-center value. Multivariate mapping inputs were therefore consistent with a streamfunction $\psi$ using the product of the

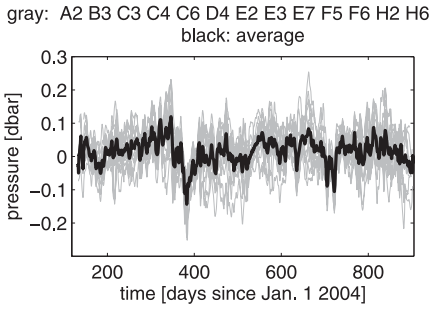


FIG. 4. Common mode (black) subtracted from bottom pressure records before mapping deep dynamical properties: 15 sites with 2-yr continuous pressure records (gray) determined the common mode as the daily average among these 15.

local Coriolis parameter $f$ and geostrophic velocity $\mathbf{u}_g$, which is horizontally nondivergent ($f\mathbf{u}_g = \hat{k} \times \nabla\psi$):

$$\frac{\partial f u_g}{\partial x} + \frac{\partial f v_g}{\partial y} = 0. \quad (1)$$

A basin-wide pressure signal termed "common mode" is also considered. Deep pressures exhibited an array-wide common mode with 0.2-dbar range on 2–30-day time scales (Fig. 4). Spectral peaks occur near 21 and 13 days (not shown). The common mode signal was likely the barotropic response to large-scale atmospheric forcing. The common mode contributed to nearly two-thirds of the deep pressure variance. The common mode was removed before mapping. Retention of the common mode would add a time-dependent array-wide constant, which has no dynamical significance for the mesoscale circulation.

Leveled pressure records have been adjusted to the same geopotential surface; once leveled, pressure gradients yielded absolute geostrophic currents. We assumed that 72-h low-passed deep pressure was in geostrophic and hydrostatic balance. Additionally, we assumed that deep thermal wind shear was weak so that bottom currents were uniform with depth through the range of array-instrument depths, 5300–6400 m. Direct velocity measurements beneath the thermocline at the tall mooring sites confirmed weak deep shears: between 2000 and 5000 m, the mean shear is zero. The differences between mean speeds through this depth interval were less than 0.3 cm $s^{-1}$, ranging among the seven KESS moorings from only +1.0 to −1.5 cm $s^{-1}$. Instruments were leveled relative to the shallowest instrument, nominally the 5300-dbar level. A different deep reference level would add an array-wide constant to each pressure record, but it would not change any dynamical interpretations.

Watts and Kontoyiannis (1990) dedrifted bottom pressure by the subtraction of a linear plus exponential fit; however, this method could not differentiate between short-term pressure drift and real ocean signals. With the KESS dataset, drift curves are refined by leveling the pressure records daily for the deployment period. The method yields a time-varying component, which was the drift curve, and a time-invariant component, which was the site-specific leveling constant. This method simultaneously dedrifted and leveled pressure measurements.

For this procedure, pressure records have tidal signals removed but the drift still included. The common mode was subtracted, because it is dynamically unimportant when working with streamfunctions. A low-pass filter with a long 30-day cutoff period was applied to pressure and current records to minimize nongeostrophic signals. Figure 5 illustrates the procedure. A nondivergent streamfunction was calculated from the current records using optimal interpolation with Gaussian correlation function with a length scale of 100 km. This correlation length scale was determined from the near-bottom pressure correlations (Fig. 7). Streamfunction $\psi$ mapped to each instrument site was converted to bottom pressure by $p_{\mathrm{cm}} = \rho\psi$, where $\rho$ is density at 5300-m depth.

The fit to the difference between the 30-day low-passed pressure record, $p_{\mathrm{cpies}}$ and $p_{\mathrm{cm}}$, was both the dedrift curve and the "leveling" constant. The difference between $p_{\mathrm{cpies}}$ and $p_{\mathrm{cm}}$ guided a linear or linear plus exponential fit (labeled D in Fig. 5b) that was subtracted from $p_{\mathrm{cpies}}$ to produce the dedrifted pressure record $p'$ (note that, for G6, which is shown in Fig. 5, a linear fit provided the best drift estimate). The process was iterated until the slope of difference between $p_{\mathrm{cm}}$ and $p'$ was smaller than $\pm 1.0 \times 10^{-5}$ dbar $day^{-1}$. With this criterion, residual error resulting from drift was less than 0.01 dbar after a 2-yr interval. The maximum drift was 0.67 dbar and 36 instruments had drifts less than 0.35 dbar. The linear plus exponential curve was then subtracted from the original bottom pressure time series. Data were then detided and low-pass filtered and subsampled at half-day intervals.

The hourly pressure record, including the drift, is shown in Fig. 5e, with the initial and final drift curves superimposed. The initial drift curve has noticeably larger exponential and linear contributions than the final drift curve determined with this new method. Had the initial drift curve been removed from the hourly pressures, some ocean signals would have been misidentified as instrumental drift.

Optimal interpolation requires that the input fields have zero mean and uniform variance. The mean bottom pressure field was determined by mapping the 16-month-long mean of the 5300-m leveled pressures. Following Bretherton et al. (1976), mapping included an estimate

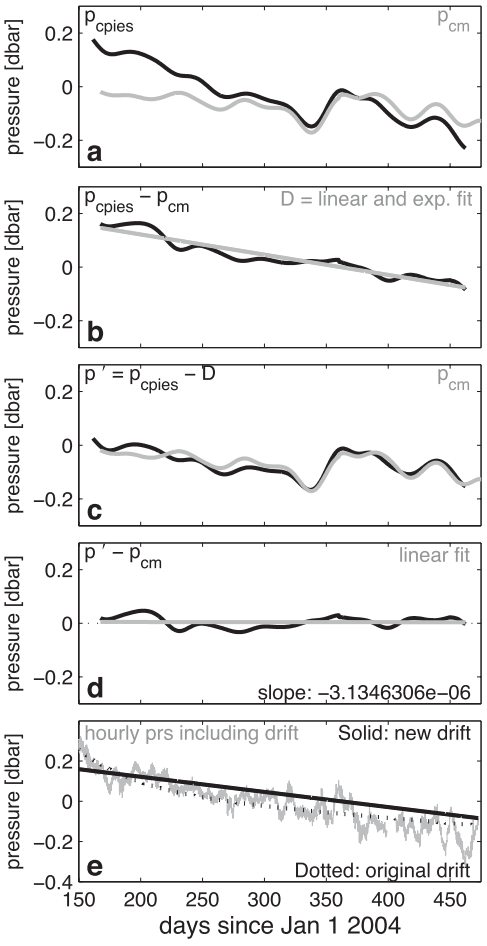


FIG. 5. Dedrift and level sequence for G6. (a) A comparison between the 30-day detided and low-pass-filtered CPIES ($p_{cpies}$ black) and the current-meter-mapped ($p_{cm}$ gray) bottom pressures indicated an instrumental pressure drift. (b) The linear and exponential fit (gray line labeled D) to the difference between $p_{cpies}$ and $p_{cm}$ (black) was the drift curve plus leveling constant. (c) The leveled and dedrifted CPIES bottom pressures ($p'$; black) are shown with the current-meter-mapped bottom pressures ($p_{cm}$; gray). (d) The difference between $p'$ and $p_{cm}$ is shown in black. The slope of the linear fit to this difference was $-3.1 \times 10^{-6}$ dbar day$^{-1}$ (gray). (e) Original hourly detided pressure record (gray) shown with the initial best guess (dotted black) and the final (solid black) drift curves.

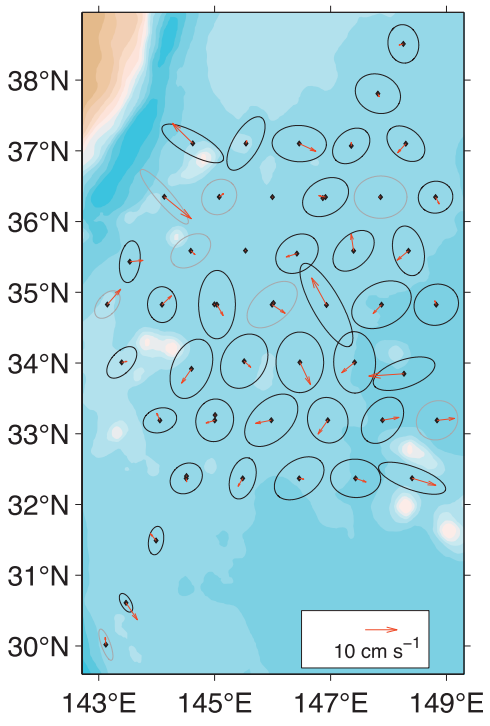


FIG. 6. Variance ellipses and mean velocity vectors for the bottom current meters averaged for the 16-month period of June 2004–September 2005. Black ellipses indicate sites with 80% or more data returned during that period, and gray ellipses indicate those with data coverage greater than 50%.

of measurement noise-to-signal variance ratios $V_n$. Error or noise associated with the pressure (current) measurements came from three sources. First, an instrument error of 0.007 dbar (1.5 cm s$^{-1}$) was included. Second, the impact of density variability on the vertical shear below 5300 m was estimated from hydrographic casts taken during the KESS field program to be on the order of 0.001 dbar (0.71 cm s$^{-1}$). Third, an error resulting from instrument position uncertainty of 0.001 25 dbar (0.13 cm s$^{-1}$) was included. This error was calculated as position uncertainty, 0.5 km, multiplied by near-bottom pressure anomaly signal, 0.20 dbar (current speed signal, 20 cm s$^{-1}$), divided by the instrument spacing. These three errors were independent of each other. The total combined error for pressure (current) was 0.0074 dbar (1.6 cm s$^{-1}$). At each site, a $V_n$ was determined for the current or pressure time series by dividing the square of the total error by the time series variance.

Near-bottom pressure and current anomalies from the mean field were the inputs to the multivariate objective mapping. The inclusion of the bottom currents in the mapping of deep fields tightened gradients. As previously stated, the multivariate mapping inputs were consistent with a nondivergent streamfunction. Six sites (B1, B2, C1, E5, F6, and H6) located near steep seamounts had rectilinear standard deviation ellipses (Fig. 6), which could indicate local wave processes; therefore, the measured currents at these sites were excluded from the mapping. Maps were produced at half-day intervals using a Gaussian correlation function with a length scale of 100 km determined from correlation function between pairs of deep pressure records (Fig. 7). Recall that the nominal array spacing was 88 km; therefore, the array spacing resolved the scales associated with the deep variability. Figure 2 reveals strong deep cyclonic and

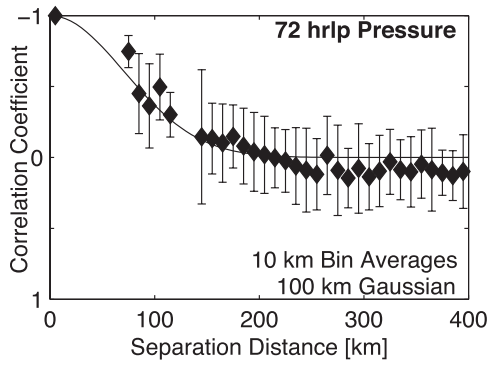


FIG. 7. Correlation function between pairs of deep pressure records determined the correlation length scale of 100 km for the Gaussian correlation function used in the mapping. Diamonds are the mean values in 10-km bins and the error bars show the std dev. A Gaussian curve with length scale 100 km is plotted with a black line. The common mode was removed from each pressure record for this calculation.

anticyclonic circulations that occurred on 28 November 2004 beneath the KE, just prior to a cold-core ring formation.

The mapping methodology of Bretherton et al. (1976) also yields a percent variance error estimate. The percent pressure variance error was dimensionalized by multiplying the pressure error by the variance of the mapped pressure product. Correspondingly, in the case of mapped currents, the percent current variance error estimate was multiplied by the mapped eddy kinetic energy. Figure 8 shows mapping errors, typical of the bottom current and pressure fields during the ''good'' 16 months. Mapped pressure (velocity) errors are typically less than 0.01 dbar (1.5 cm $s^{-1}$).

## 4. Mapping $\tau$ and $\tau$-derived fields

Round-trip acoustic travel time measured by the inverted echo sounder allowed estimates of vertical profiles of temperature, salinity, and density utilizing empirical relationships established with historical hydrography. This is the GEM representation (e.g., Meinen and Watts 2000): a lookup table for hydrographic properties indexed by $\tau$ integrated between the surface and a preselected reference depth $\tau_{\text{index}}$. In this section, descriptions of the choice of $\tau_{\text{index}}$ (section 4a) and the construction of the empirical relationships (section 4b), the conversion of measured $\tau$ to $\tau_{\text{index}}$ (section 4c), and the methodology that maps $\tau_{\text{index}}$ (section 4d) and absolute full-water-column geostrophic velocities (section 4e) are given.

### *a. Dynamic $\tau$*

In an analogy with dynamic height, a dynamic $\tau$ that was independent of a latitudinal dependence of gravity (Watts et al. 2001b) was determined. This allowed the use of hydrographic stations from different latitudes to construct the GEM table. Round-trip travel time $\tau$ between the surface and a reference pressure $p_{\text{ref}}$ is defined by

$$\tau = \int_0^{p_{\text{ref}}} \frac{2}{c\rho g}\, dp', \tag{2}$$

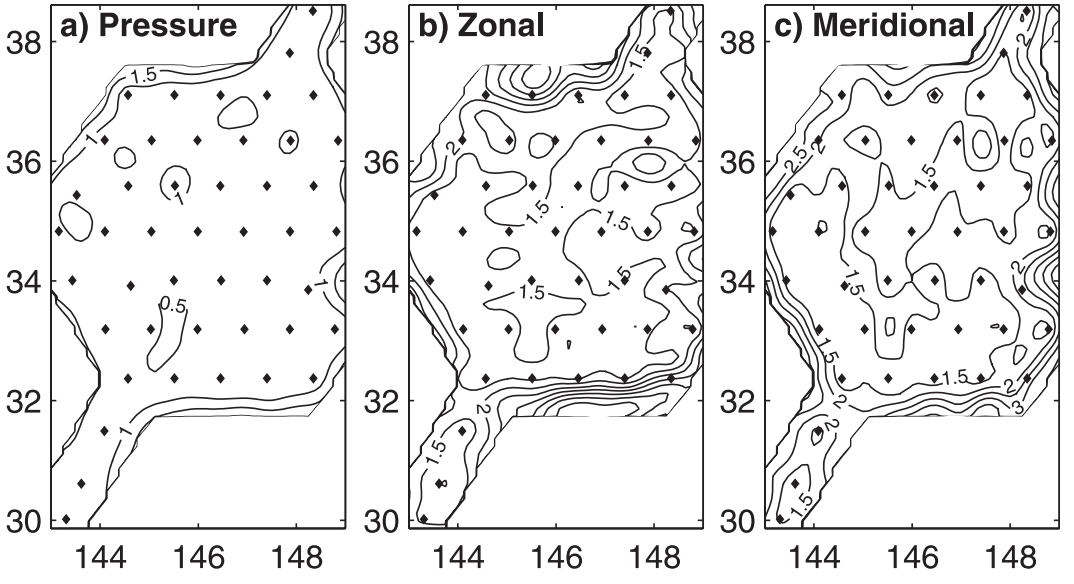


FIG. 8. Mapping errors associated with (left) deep pressure and (middle) zonal and (right) meridional velocity for 28 Nov 2004; they are typical of the 16-month mapping period from June 2004 to September 2005. (left) Pressure is in dbar $\times 10^2$ and (middle) zonal and (right) meridional velocities are in cm $s^{-1}$.

where $c$ is the speed of sound and $\rho$ is density. Acceleration due to gravity $g$ depends on both latitude and depth. Two hydrocasts with identical water properties can differ by the order of 5 ms within the KESS region because of the dependence of gravity on latitude. A simple solution was to calculate a $\tau$ that was independent of latitude by using a constant value for $g$ of 9.8 m s$^{-2}$.

For conformity, $\tau$ measured by the IESs was converted to dynamic $\tau$ by the following empirical approach, similar to that found in Baker-Yeboah (2008): Gravitational acceleration's depth $z$ and latitude $\lambda$ dependence were separated,

$$g(\lambda, z) = G(\lambda)H(z), \tag{3}$$

and $G(\lambda)$ was taken outside the integral,

$$\tau = \frac{1}{G(\lambda)} \int_0^{p_{\text{ref}}} \frac{2}{c\rho H(z)} dp'. \tag{4}$$

In addition, $1/H$ was also taken out of the integral as an average ($\overline{1/H}$), and $p_{\text{ref}}$ was set to $P_b$, the average measured bottom pressure at the site,

$$\tau = \frac{1}{G(\lambda)} \overline{\left(\frac{1}{H}\right)}_{P_b} \int_0^{P_b} \frac{2}{c\rho} dp'. \tag{5}$$

Historical hydrography empirically determined $\overline{(1/H)}_{P_b}$ as

$$\overline{\left(\frac{1}{H}\right)}_{P_b} = \frac{g(\lambda, 0)}{9.8} \left(\frac{\tau}{\text{dynamic-}\tau}\right), \tag{6}$$

and it yielded the following expression to convert measured $\tau$ to dynamic $\tau$:

$$\text{dynamic-}\tau = \tau \left[ \frac{g(\lambda, 0)}{9.8\left(1 - \dfrac{P_b}{1.017 \times a}\right)} \right], \tag{7}$$

where the radius of the earth $a$ is 6371 km. The depth- and latitude-dependent scale factor in square brackets in Eq. (7) is accurate to 6 ppm for depths 0–6000 dbar.

### b. Gravest empirical mode

Four data sources contributed to the historical hydrographic database (Fig. 9) used to create the lookup tables: hydrocasts taken during the KESS field experiment; Argo float profiles (available online at http://www.usgodae.org); and hydrocasts obtained from two climatologies, Japan Oceanographic Data Center (available online at http://www.jodc.go.jp) and North Pacific Hydrobase (available online at http://www.whoi.edu/science/PO/hydrobase; MacDonald et al. 2001). Neither bottle data nor casts before 1998 were included in the database in order to avoid integration over coarse vertical resolution and to avoid possible secular changes in water properties. The resolution in space and time of year was uniform in coverage with some emphasis on the southeast, because profiling floats initially deployed in the recirculation gyre tended to remain trapped within the gyre. Float profiles constituted the largest fraction of the database (2069 of 3814 casts); their measurements were concentrated during 2004–06 and typically reached 1400 dbar. They provided a fairly even distribution throughout the year. Details of the float-data quality control that utilized a local climatological temperature–salinity curve are discussed in Qiu et al. (2007).

The integration upper limit of 0 dbar and lower limit of 1400 dbar for $\tau_{\text{index}}$ (or alternatively $\tau_{0\text{–}1400}$) were chosen to meet two needs: capture the thermocline and retain a large number of casts. Because $\tau_{\text{index}}$ encompassed the seasonal thermocline, each hydrocast was deseasoned (Tracey and Watts 1986; Watts et al. 2001b). The seasonal cycle in the database had insignificant signal below 250 dbar. A spline was fit relating $\tau_{0\text{–}250}$ to $\tau_{250\text{–}1400}$ (Fig. 10, top). The seasonal signal was the residual from this curve. To compute the annual progression, the residuals were grouped into 15-day overlapping bins (50% overlap) and averaged. The resulting curve (Fig. 10, bottom) was smoothed using a low-pass filter with a 100-day cutoff period. The amplitude of the seasonal cycle was 1 ms, with an rms residual of 0.66 ms (Fig. 10).

To construct the lookup tables, the hydrocasts were first sorted by deseasoned $\tau_{\text{index}}$; then temperature $T(p)$, salinity $S(p)$, and specific volume anomaly $\delta_n(p) = \int 1/\rho \, dp$ profiles were interpolated onto a $\tau_{\text{index}}$ versus pressure grid (Figs. 11–13). Following Meinen and Watts (2000), a cubic smoothing spline was fit at distinct pressure levels. The pressure grid resolution was 20 dbar from the surface to 1000 dbar, 40 dbar from 1000 to 1200 dbar, 80 dbar from 1200 to 2400 dbar, 100 dbar from 2400 to 3000 dbar, and 200 dbar from 3000 to 6000 dbar. The decrease in data density with depth justified a decrease in the vertical resolution of the pressure grid and allowed the smoothing parameter in the cubic spline to decrease with depth. At the deepest levels, greater than 5500 dbar, the resulting spline curves were horizontal reflecting the nearly uniform properties of the deep North Pacific. That the appropriate amount of smoothing was performed was verified by replicating the procedure described in Sun and Watts (2001) to determine the a priori error in streamfunction space.

There are systematic relationships between $\tau_{\text{index}}$ and vertical profiles of temperature, salinity, and $\delta$ (Figs. 11–13). Not only does $\tau_{\text{index}}$ organize integral quantities, such as

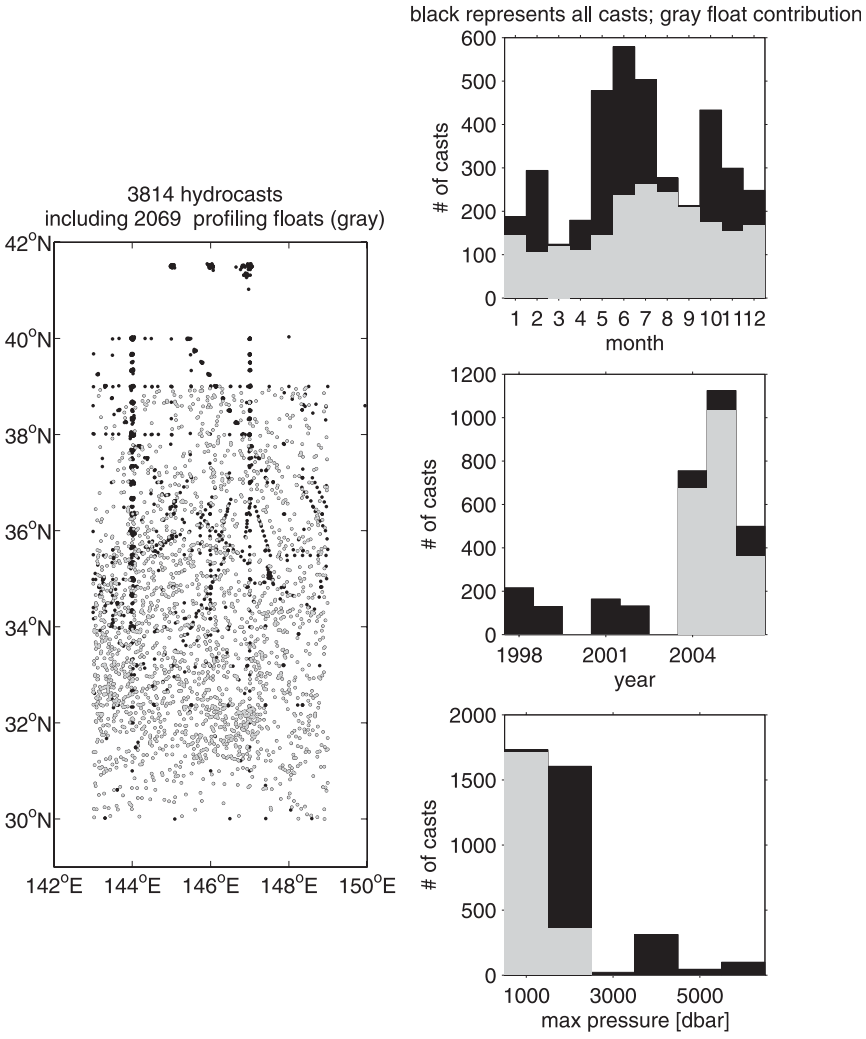


FIG. 9. Hydrographic dataset used to construct the seasonal cycle, the GEM lookup table, and the conversion between $\tau_{\text{index}}$ and measured $\tau$. (right) Histograms of (top) cast month, (middle) year, and (bottom) pressure. Float profiles—represented by (left) gray dots and (right) gray bars—constitute a large fraction of the dataset. (left) Map of station locations.

heat content and dynamic height, as originally envisioned by Rossby (1969) and Watts and Rossby (1977), but in strong-jet environs like the KE $\tau_{\text{index}}$ can be a proxy for vertical profiles of temperature, salinity, and $\delta$. This is a GEM; small-vertical-scale intrusions and intrathermocline eddies will not be represented. However, the GEM captures more than just the depth of the thermocline; for example, the temperature GEM shows the warm salty surface Kuroshio surface core and 17°C mode water at low $\tau_{\text{index}}$. The salinity and temperature structures associated with North Pacific Intermediate Water are evident at the long values of $\tau_{\text{index}}$.

The KESS GEM fields estimated temperature (salinity) at 500 dbar in the thermocline with rms error of 0.45°C (0.09 psu). The rms error decreased with depth (Figs. 11–13) and at 2000 dbar was less than 0.06°C (0.01 psu). The highest rms errors were near the surface, particularly at large $\tau_{\text{index}}$ values that corresponded to cold subpolar waters. In addition, there was a ''tongue'' of high rms that extended from near surface at long $\tau_{\text{index}}$ to near 700 dbar at shorter $\tau_{\text{index}}$ (near 1.86 s). This came about because of an increase in vertical intrusions at the core of the KE.

Deep variability in temperature and salinity in the KESS regions is quite weak (Fig. 14); however, sorting profiles by $\tau_{\text{index}}$ also organizes the deep variability. The ''steps'' in deep temperature and salinity below 4000 dbar are an artifact of the decrease in the number of deep hydrocasts available and indicate cruise-to-cruise calibrations different by 0.003°C.

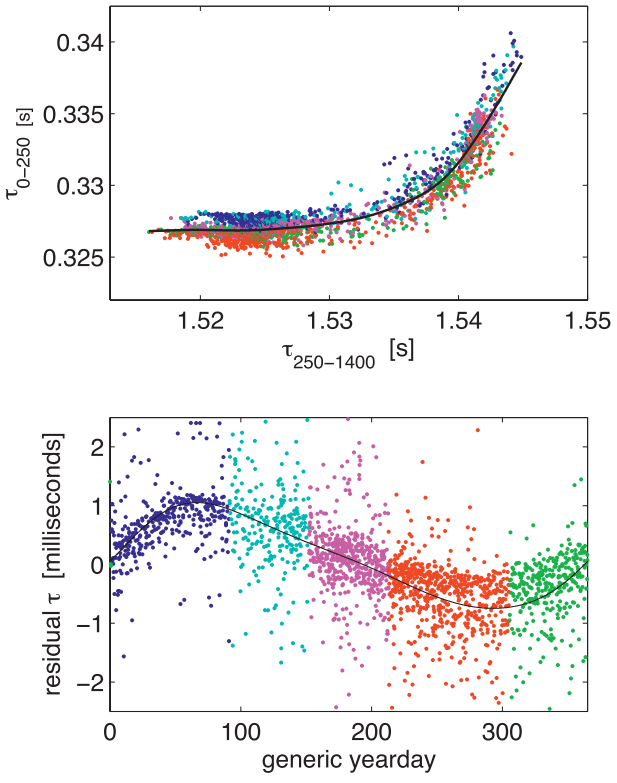


FIG. 10. (top) The dependence of acoustic travel time through the upper 250 dbar upon $\tau_{250-1400}$ calculated from hydrography. The black line shows the fitted spline. (bottom) After removing the spline fit, the residuals are plotted vs day of year (dots). The seasonal curve (black line) is subtracted from dynamic $\tau$ to create a deseasoned dynamic $\tau$. The samples are color coded by generic yearday.

Following the methods of Watts et al. (2001b), the seasonal signal was also determined for temperature, salinity, and specific volume for the upper water column (0–250 dbar). Here, we show the temperature seasonal signal (Fig. 15), together with an example of the spline fit and residuals at the 90-dbar level. The seasonal signal was determined by sorting the residual from the spline fit as a function of yearday and applying a 100-day fourth-order Butterworth low-pass filter. The temperature (salinity) signal range was largest at the surface, 10°C (0.24 psu), and it decreased to 2°C (0.04 psu) at 100 dbar and 0.2°C (0.016 psu) at 250 dbar. The seasonal signal was asymmetric with yearday; winter cooling occurred faster than summer warming. Likewise, wintertime freshening was more abrupt than salinity increases during the summer. Note that only float data were used to construct the seasonal signal and generate a seasonal signal contemporary with KESS. Our assumption here was that the seasonal signal was spatially uniform across the array. A more sophisticated methodology would account for regional variability; however, in a strongly meandering current, the approach would need to be a function of streamfunction (or $\tau_{\text{index}}$) rather than latitude or longitude.

### c. *Measured* $\tau$ *to* $\tau_{\text{index}}$

Measured $\tau$ must be converted or calibrated to $\tau_{\text{index}}$ to utilize the GEM lookup tables. Several steps corrected measured $\tau$ to dynamic $\tau$ and finally to $\tau_{\text{index}}$. The $\tau_{\text{index}}$ is the purely steric deseasoned dynamic $\tau$ calculated from hydrographic data as described in section 4a. Steric dynamic-$\tau$ records are created from CPIES-measured $\tau$ by subtracting the contribution of mass changes to pathlength, $2p/(\rho g c)$, where $p$ is the instrument's dedrifted but not detided bottom pressure. Maximum deep pressure variability of 0.2 dbar contributed mass-loading roundtrip travel times near 0.02 ms. Steric $\tau$ was next converted to dynamic $\tau$ with Eq. (7). Measured $\tau$ varied in response to seasonal warming and cooling of the surface layers. To minimize these seasonal fluctuations, a seasonal cycle was removed from each dynamic-$\tau$ time series (Fig. 10).

In previous experiments (e.g., Meinen and Watts 1998), the final conversion from measured dynamic $\tau$ to $\tau_{\text{index}}$ consisted of determining a linear relationship between a GEM $\tau_{\text{index}}$ and a deep (near bottom) $\tau$. The slope would be calculated by historical hydrography, and for each instrument site a calibration hydrocast would determine the intercept (typically, the cast is taken at the instrument site while the instrument measures $\tau$).

The methodology for KESS accounts for the nonlinear relationship between measured $\tau$ and $\tau_{\text{index}}$ and sparse deep hydrocasts. A polynomial relationship between $\tau_{\text{index}}$ and $\tau_{0-4000}$ was determined empirically (Fig. 16) from the deseasoned historical hydrography (Fig. 9). There were enough deep-reaching casts to construct a $\tau_{\text{index}}$ and $\tau_{0-\text{deep}}$ curve for depths as deep as 4000 dbar. This curve deviates from a linear relationship by as much as 0.5 ms for low $\tau_{\text{index}}$ values ($<$5.249 s). Deep ($>$4000 m) North Pacific properties exhibit weak vertical gradients in temperature and salinity, and many investigators (including ourselves) have opted for partial-water-column casts. Therefore, an assumption was made that the only difference between $\tau_{0-4000}$ and deeper $\tau$ was due to a longer pathlength, which merely offsets the curve in Fig. 16 for different depths, rather than change its slope or higher derivatives.

Hydrocasts taken at CPIES sites and then converted to $\tau_{0-4000}$ created calibration offsets that were added to the time series of deseasoned dynamic $\tau$. Most sites had at least two calibration casts, and the offset was determined as their average. The final step scaled measured steric dynamic deseasoned $\tau_{0-4000}$ to $\tau_{\text{index}}$ using the polynomial curve shown in Fig. 16.

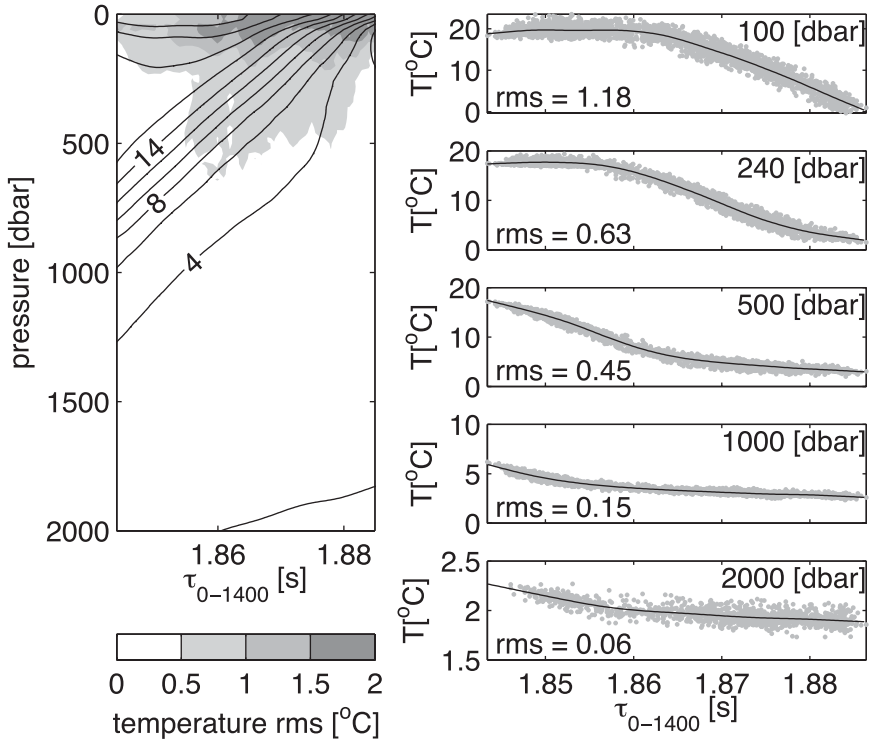


FIG. 11. (left) Contour plot of the cubic smoothing spline fits for the temperature GEM field. The rms of fit between data and the spline fit are shaded contours. The temperature gradients below 2000 dbar are weak and are not shown. (right) Scatterplot of temperature vs $\tau_{\text{index}}$ (gray dots) for five representative pressure levels with the fitted splines superimposed (black line). The rms of each fit is noted in the bottom left.

Errors derived from six sources: 1) uncertainty in the scatter in the $\tau$ low-pass measurement of 0.05 ms, 2) the mass-loading contribution of 0.02 ms, 3) the conversion from $\tau$ to dynamic $\tau$ of 0.05 ms, 4) the seasonal correction of 0.66 ms, 5) the conversion from dynamic $\tau$ to $\tau_{\text{index}}$ of 0.7 ms, and 6) the calibration curve $\tau_{0–1400}$ and $\tau_{0–4000}$ of 0.34 ms. The error associated with the conversion from $\tau$ to dynamic $\tau$ (the third error source) includes contributions from a possible spatial offset between the hydrocast and IES, internal tide variability, deep density variability beneath 4000-m depth, error in deseasoning, and error in the dynamic-$\tau$ calculation. Combining these six independent errors yielded an uncertainty of 1.02 ms in IES-measured $\tau_{0–1400}$. Comparisons with $\tau_{0–1400}$ measured by the profiling floats agreed within this level of error (see section 5).

### *d. Maps of* $\tau_{\text{index}}$

Maps of $\tau_{\text{index}}$ were also produced with optimal interpolation techniques adapted from Bretherton et al. (1976). An iterative mapping procedure was employed that first mapped a low-frequency large-scale field and then mapped the anomaly from that field (Tracey et al. 1997). The frequency cutoff of $^1/_{60}$ day$^{-1}$ between these scales was determined by $\tau_{\text{index}}$ spectra, which indicated a spectral gap near 60 days with roughly 80% of the signal variance contained in the low-frequency range. Correlations between pairs of instruments for 60-day low-pass (high pass) $\tau_{\text{index}}$ records suggested that a length scale of 130 km (75 km) was appropriate for the Gaussian correlation function (Fig. 17). Several other cutoff frequencies ($^1/_{15}$, $^1/_{30}$, and $^1/_{45}$ day$^{-1}$) and their corresponding correlation length scales were tested. Mapping results were insensitive to these choices.

First, a broad-scale time mean was mapped using the record-length mean $\tau_{\text{index}}$ time series from the instruments using a correlation length scale of 200 km. In addition, a far-field mean was prescribed along the array perimeter out to a distance of one-half correlation length scale. Generalized Digital Environmental Model (GDEM) climatological geopotential (Teague et al. 1990) converted to $\tau_{\text{index}}$ via the GEM lookup tables was used for this far-field mean.

The low-frequency, large-scale mapped field, called the daily mean, resulted from the optimal interpolation of the 60-day low-pass $\tau_{\text{index}}$ time series residuals from

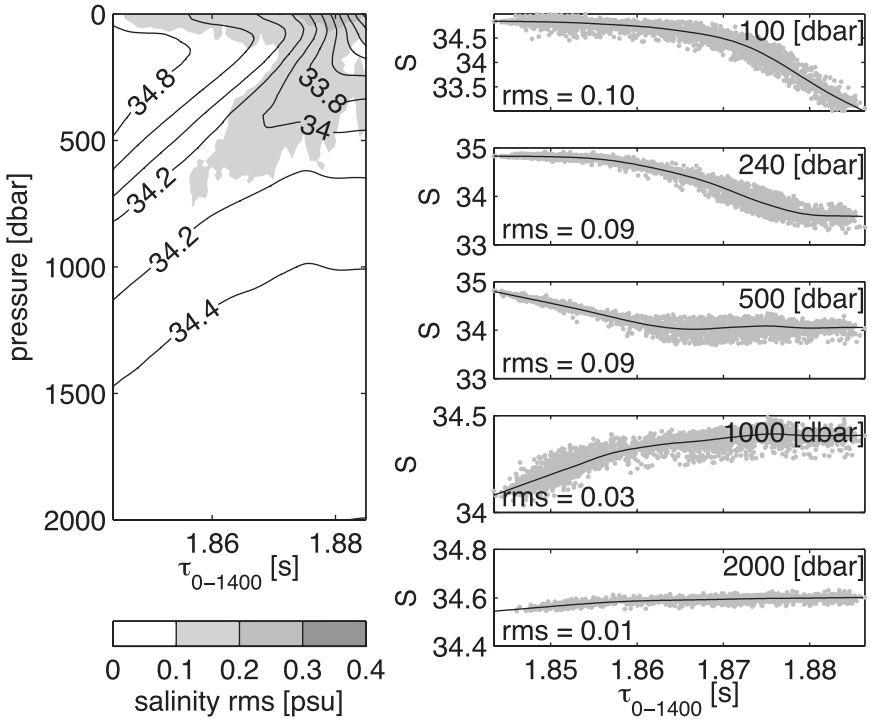


FIG. 12. As in Fig. 11, but for salinity.

the broad-scale time-mean map using a correlation length scale of 130 km. Note that Tracey et al. (1997) use the term ''first guess'' for the daily-mean fields. A daily anomaly map was constructed by mapping the residual of the $\tau_{\text{index}}$ time series from the daily-mean fields. The final daily map was the sum of daily mean and daily anomaly map (technically, these maps are constructed at one-half-day intervals).

The optimal interpolation input noise-to-signal parameter $V_n$ was determined site by site. The signal was straightforward to calculate as the variance of the input time series. The noise estimate was derived from our $\tau_{\text{index}}$ errors. The two-step adaptive mapping process required an error assignment appropriate to the input time series, and the $\tau_{\text{index}}$ error of 0.96 ms assigned to the daily mean included the error from $\tau$ scatter in the 60-day low-pass time series, the error from the deseasoning process, and the error from the conversion from measured $\tau$ to dynamic $\tau$ as well as the conversion from dynamic $\tau$ to $\tau_{4000}$. The $\tau_{\text{index}}$ error of 0.34 ms assigned to the daily anomaly map included the $\tau$ scatter in the 3-day low-pass time series and the errors associated with the steric correction and the conversion from $\tau_{0\text{–}4000}$ to $\tau_{\text{index}}$.

Dimensional errors were recovered by scaling the optimal interpolation percent variance error by the variance of the mapped field. The errors in the daily mean and the daily anomaly map were considered to be independent. Once $\tau_{\text{index}}$ was mapped, the scalar quantities, temperature, salinity, and specific-volume anomaly on any desired pressure level were looked up in the GEM tables. The scalar mapped error fields have uncertainty because of the scatter in the GEM field and the error in $\tau_{\text{index}}$.

Figures 18 and 19 show typical mapping errors during the 16-month period. Temperature error was highest near site D3, which had no data during the first year. Temperature variance and hence mapped errors were lowest on the equatorward side of the KE core. Mapped temperature errors decreased with depth (1.5°C at 300 m, 0.3°C at 600 m, and <0.1°C below 1200 m).

### e. Geostrophic shear

Geopotential height was readily integrated from the specific volume anomaly GEM profiles, as indexed by $\tau_{\text{index}}$ (geopotential anomaly $\Phi(p, \tau_{\text{index}}) = \int_p^{p_r} \delta(p', \tau_{\text{index}})\, dp'$, where $p_r = 5300$ dbar). Geostrophic shears were calculated with the methods of Sun and Watts (2001). Their discussion is repeated here to reinforce that the vertical structure of these geostrophic shears is equivalent barotropic (it is in the same direction throughout the water column):

$$fu_g = -\frac{\partial \Phi(p, \tau_{\text{index}})}{\partial y} = -\frac{\partial \Phi(p, \tau_{\text{index}})}{\partial \tau_{\text{index}}} \frac{\partial \tau_{\text{index}}}{\partial y} \quad \text{and} \tag{8}$$

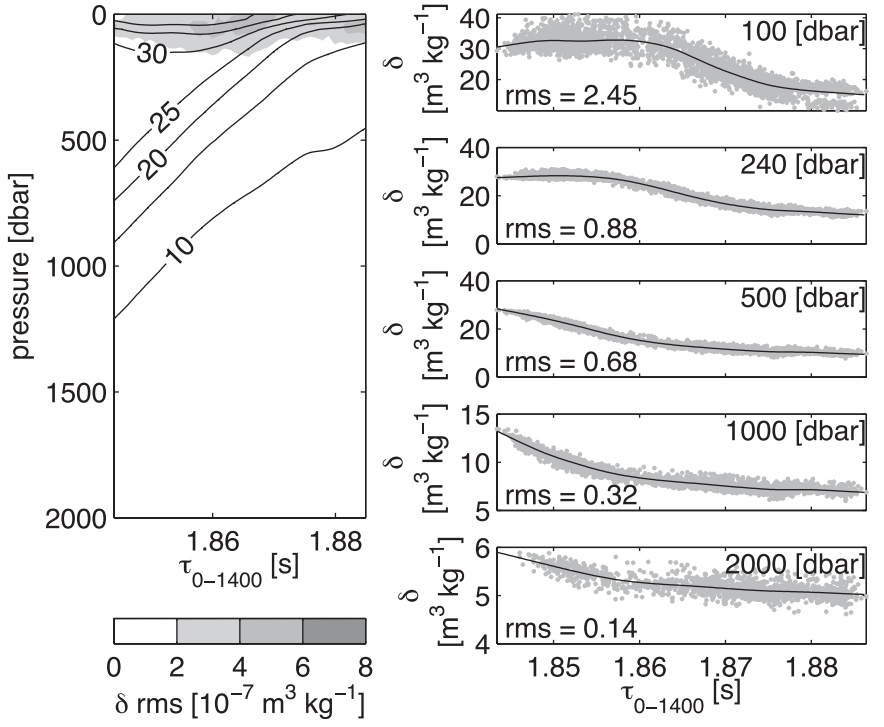


FIG. 13. As in Fig. 11, but for specific volume anomaly $\delta$ in $m^3\ kg^{-1}$.

$$fv_g = \frac{\partial \Phi(p,\ \tau_{\text{index}})}{\partial x} = \frac{\partial \Phi(p,\ \tau_{\text{index}})}{\partial \tau_{\text{index}}} \frac{\partial \tau_{\text{index}}}{\partial x}. \quad (9)$$

Because $u_g/v_g$ is a function of $\tau_{\text{index}}$ only and this holds for all depths, flow is parallel with depth. By using the right-hand side of Eqs. (8) and (9), the mapped $\tau_{\text{index}}$ fields determine the baroclinic velocity at any depth. Geostrophic shears were determined from the $\tau_{\text{index}}$ gradient of the $\Phi$ GEM multiplied by the $\tau_{\text{index}}$ spatial gradients. Spatial gradients of $\tau_{\text{index}}$ were calculated through iterative optimal interpolation mapping in the same manner as described in section 4d. Error in the shears was determined by propagating the $\delta$ GEM error and $\tau_{\text{index}}$ gradient mapping error through Eqs. (8) and (9).

Combining upper and lower ocean maps produced absolute velocities throughout the water column. Upper-ocean relative velocities were created by mapping velocities referenced to zero at 5300 dbar. The 5300-dbar-level velocities created with the bottom pressure and current-meter records then served to reference these upper-ocean relative velocities.

Figures 18 and 19 show typical mapping errors during the 16-month mapping period for the absolute geostrophic velocity. Velocity errors were highest in regions of strong eddy kinetic energy, within and south of the jet core. Velocity errors decreased with depth and mapped errors were typically near 12 cm $s^{-1}$ (8 cm $s^{-1}$) near 500-m (800 m) depth. Note that we have chosen to show the vertical profile of estimated error in the jet core (Fig. 19) where the errors were highest as well as north of the jet core. These errors correspond to our expected

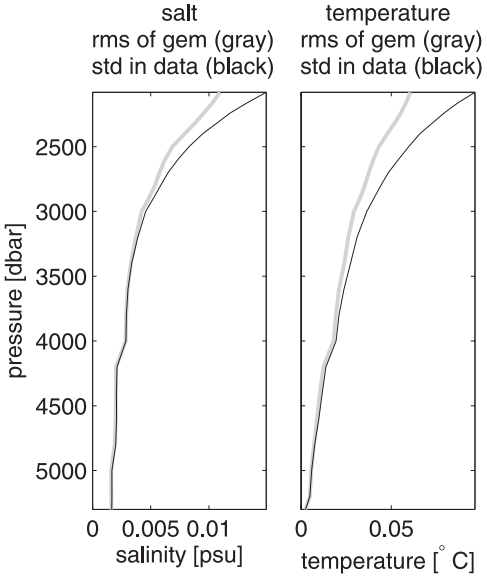


FIG. 14. Deep (right) temperature and (left) salinity variability are very small in the North Pacific (black lines). The GEM field (gray) organized this data a bit (note reduction in rms); however, below 3000 dbar, deep temperature and salinity variability is within the limit of temperature and salinity calibrations.

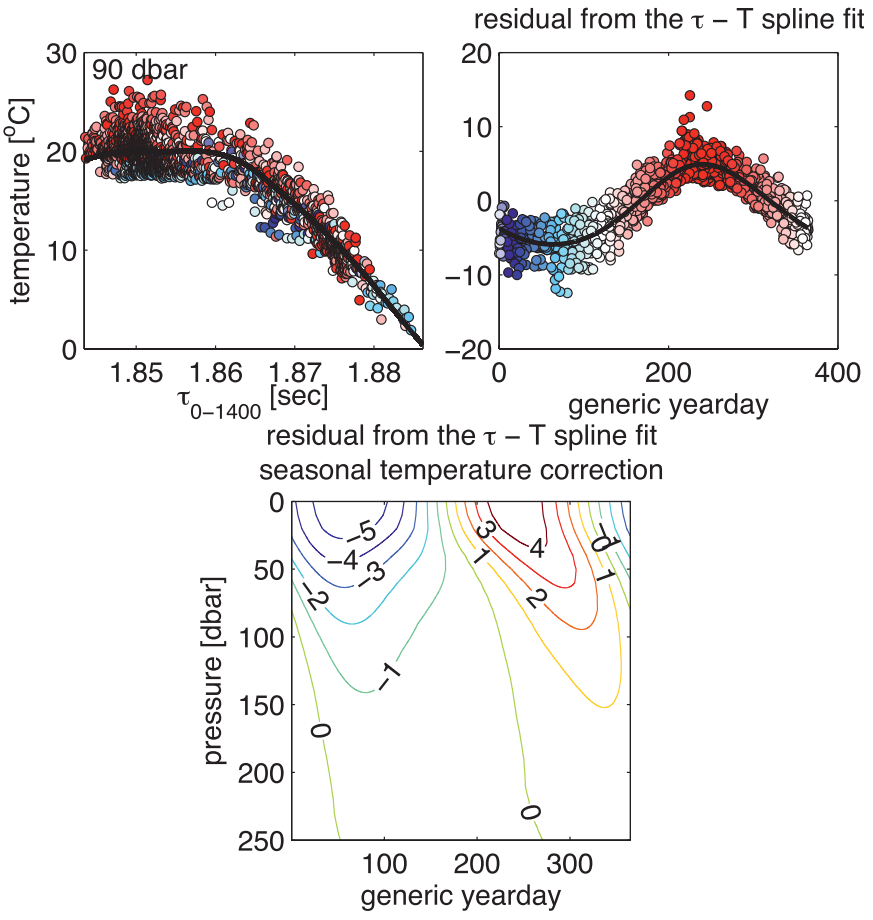


FIG. 15. (top left) Scatterplots of profiling float temperature vs $\tau_{\text{index}}$ at 90 dbar with the cubic spline fit shown as a solid dark line. All samples are color coded by generic yearday transitioning from blue in winter to red in summer. (top right) A clear seasonal signal in temperature emerges when the residuals from the spline fit are sorted by time of year. (bottom) Seasonal temperature corrections calculated at 10-dbar increments from the surface to 250 dbar are contoured as a function of yearday and pressure. The temperature seasonal correction ranges through more than 9°C at the surface and decays to less than 0.1°C by 250 dbar.

difference between mapped and pointwise velocity measurements, which include submesoscale and ageostrophic components. The error in the average geostrophic velocity between CPIES is smaller and near 10 cm $s^{-1}$ at the surface (gray lines in Fig. 19, right). This error was determined by propagating the error in geopotential height through the geostrophic equations, and it accounted for the 0.5 correlation between adjacent CPIES sites.

To place these errors in context, error estimates will be needed for volume transport and potential vorticity from the KESS array. The mean geostrophic velocity error from the surface to 6000 m over a characteristic KE width of 200 km is about 2.0 cm $s^{-1}$. The corresponding instantaneous transport error estimate is 24 × $10^6$ $m^3$ $s^{-1}$. The annual-mean KE transport, using an integral time scale of 20 days, can be estimated with 6 × $10^6$ $m^3$ $s^{-1}$ error, which is considerably smaller than the total KE transport ≈100 × $10^6$ $m^3$ $s^{-1}$ (e.g., Yoshikawa et al. 2004). Thickness vorticity error can be expressed as $\nabla H/Hf$, where $H$ is layer thickness and $\nabla H$ represents uncertainty in thermocline depth. Using $\nabla H \approx 30$ m, an upper-layer $H \approx 600$ m, and a lower-layer $H \approx 6000$ m, the upper- and lower-layer thickness vorticity errors are therefore $0.05f$ and $0.005f$, respectively. Similarly, relative-vorticity error is approximately $u_e/L$, where $u_e$ and $L$ are characteristic velocity and length scales. At 500-m depth, a $u_e$ of 12 cm $s^{-1}$ and $L$ of 100 km lead to an error of $0.015f$. Below 800 m, $u_e$ is less than 8 cm $s^{-1}$ and the relative-vorticity error becomes $0.01f$.

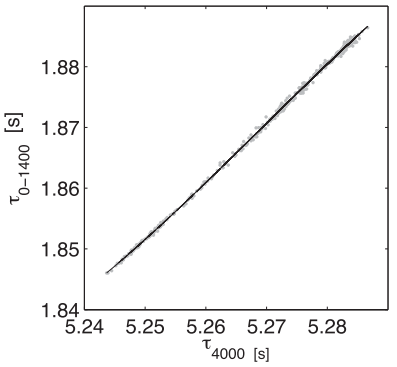


FIG. 16. Polynomial curve fit (black line) between $\tau_{0-4000}$ and $\tau_{0-1400}$ calculated from hydrographic measurements (dots) in the KESS region with seasonal variations removed.

## 5. Evaluation

### *a. Float* $\tau_{\text{index}}$

Profiling float hydrocasts provided independent estimates of the $\tau_{\text{index}}$ calibration and mapping error. For this comparison, $\tau_{\text{index}}$ calculated from each profile was deseasoned, and the $\tau_{\text{index}}$ map nearest in time was interpolated to the float's location. Then, the measured and mapped values were differenced for each profile. Two comparisons emphasize (i) how well a few profiles that surfaced near CPIES agree and (ii) how well the many profiles within the well-mapped region agree. A total of 54 floats within 10 km of a CPIES or PIES site yielded an rms difference between measured and mapped $\tau_{\text{index}}$ of 0.95 ms, which agrees favorably with our predicted error estimate of 1.02 discussed in section 4c. Measured and mapped $\tau_{\text{index}}$ compare well: the rms difference from 1238 hydrocasts within 60 km of the nearest instrument was 1.65 ms. The comparison did not reveal any spatial or temporal biases (which would have indicated $\tau$ calibration problems). The rms differences are compared in Fig. 20 to estimated mapping error. There is nearly a one-to-one correspondence, which confirms our estimation. For regions with low mapping error, the actual rms differences were slightly higher (by 0.27 ms) than predicted. This was likely because the float measurement itself has error. In practice, regions with $\tau_{\text{index}}$ error greater than 2.5 ms were masked (like that shown in Fig. 2).

### *b. McLane moored-profiler temperature profiles*

McLane moored-profiler temperature records provide another independent dataset available for comparison. The moorings were designed to sample temperature, conductivity, pressure, and velocity from nominally 1500 to 250 to 1500 dbar every 15 h. In strong current events, sampling gaps occurred not only because of mooring drawdown but also because the profiler struggled to complete the round-trip. Moorings K1–K7 had either a CPIES or PIES within a 6-km distance, except for K4, which was 44 km from E4 during the first year. Mooring K1 was excluded from this comparison because the upper water column was not measured during the first year.

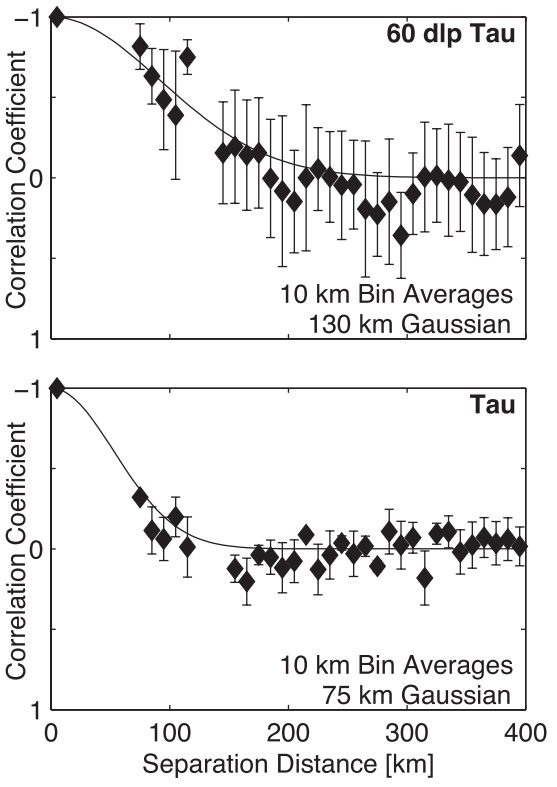


FIG. 17. Correlations between pairs of instruments for the 60-day (top) low-pass and (bottom) high-pass $\tau_{\text{index}}$ records are shown. Diamonds are the mean values in 10-km bins, and the error bars show the standard deviation. Gaussian curves with length scales of (top) 130 and (bottom) 75 km are shown by the black lines.

For this temperature comparison, linear interpolation filled the MMP data across gaps less than 2 days. These were low-pass filtered using a fourth-order Butterworth filter with a cutoff period of 7 days; all segments longer than 50 days were retained (CPIES mapped temperatures were similarly low-pass filtered for the comparisons).

Overall, the temperature time series at 500 dbar track each other well (Fig. 21; K1, K3, and K6 not shown). Typically, the rms temperature difference was 0.5°C, which is in agreement with error estimates. These errors derive mainly from scatter within the GEM table. The slightly higher rms differences and error estimates at K4 result from the substantially increased distance between the MMP and CPIES sites.

Vertical profiles of temperature can also be compared over the depth range of the MMP. The moored-profiler and CPIES-estimated profiles for 4 August 2004 (relative

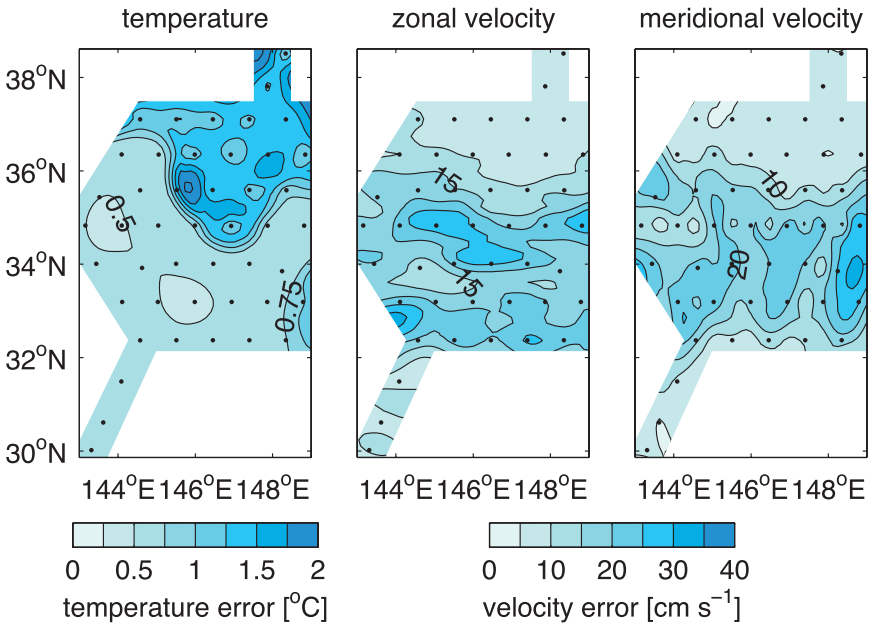


FIG. 18. Maps of estimated optimal interpolation error at 200-m depth for (left) temperature and total (middle) zonal and (left) meridional velocity during the good mapping period. Mapped temperature error was highest near site D3, which had no data during the first year. Temperature variance and hence error were lowest on the equatorward side of the KE core.

yearday 216) superimposed in Fig. 22 are in good agreement. This figure highlights that the CPIES methodology captured the low (or gravest) mode structure. The MMP up and down traces exhibit short-term and small-scale variability (filaments or intrusions) that cannot be reproduced by the GEM methodology.

Figure 23 quantifies the rms difference between moored-profiler and CPIES temperature estimates as

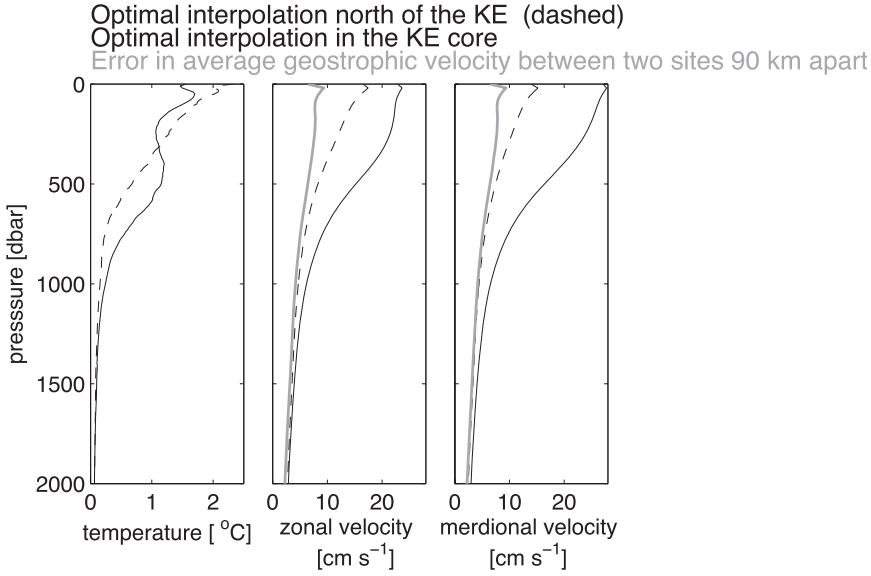


FIG. 19. Vertical profile of estimated optimal interpolation error for (left) temperature and (middle) zonal and (right) meridional velocity for the good mapping period at the KE core (midpoint between sites E5, E6, and F5; solid black line) and north of the KE core (midpoint between sites D5, D6, and C5; dashed black line). The gray line in (middle), (right) shows the error in the average geostrophic velocity between two sites 90 km apart.

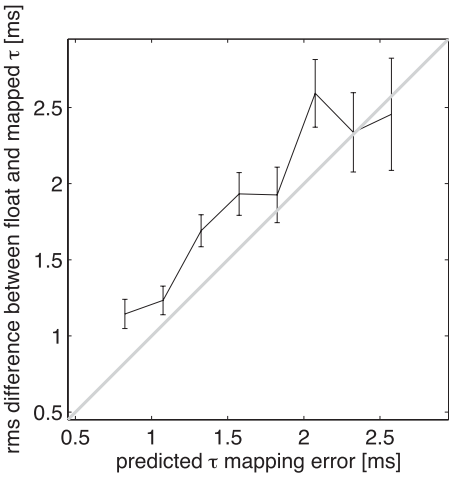


FIG. 20. The $\tau_{\text{index}}$ errors determined from profiling float hydrocasts agree well with predicted mapped $\tau_{\text{index}}$ errors. The rms differences averaged in 0.25-ms bins are plotted against estimated mapping error. The error bar for each bin is calculated as the std dev computed over rms differences between 0 and 2.7 ms divided by the square root of the number of estimates in the bin.

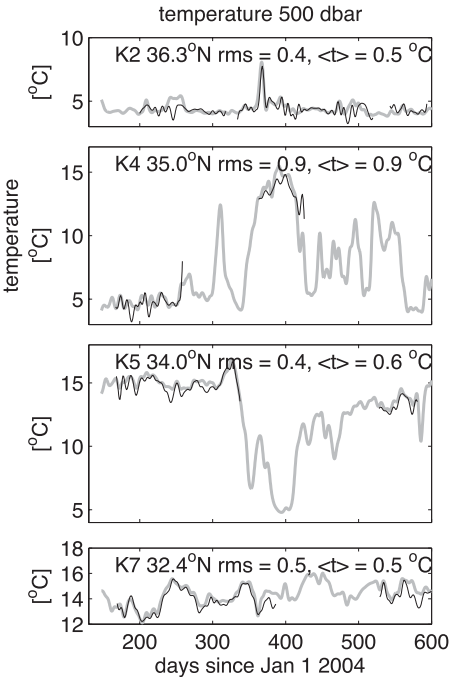


FIG. 21. Comparison between temperature measurement at 500 dbar by the MMPs (black lines) and estimates from CPIES maps (gray lines) for (top)–(bottom) K2, K4, K5, and K7. For comparison, both datasets were low-pass filtered with a 7-day fourth-order Butterworth. Only MMP segments greater than 50 days with gaps less than 2 days linearly interpolated were retained. The rms difference between each time series is shown at the top. The expected error is written as $\langle t \rangle$.

a function of depth for the good mapping period. Again, the largest errors occurred at K4. Encouragingly, estimated errors agree with the observed rms difference between the two types of measurements.

### c. ADCP 200-dbar velocity measurements

The ADCP at the top of the MMPs provided independent velocity measurements to evaluate mapped velocities and error estimates. Three sites were not included in this comparison: sites K1 and K8 had no data for the first year and site K3 was adjacent to CPIES site D3, which did not return data for the first year. The ADCPs did not have a pressure recorder. To determine the pressure or depth of the instrument as a function of time, either the minimum pressure of the MMP or an estimate of depth from the ADCP surface echo return was used. Mooring draw down reached over 300 m (L. Rainville 2009, personal communication).

The 3-day low-pass time series at the 200-dbar level track each other well (Fig. 24). The rms differences are typically near 20 cm $s^{-1}$. Note that the CPIES estimates and the measurements were not expected to agree perfectly, because the former was a mapped value whereas the latter was a point measurement. Furthermore, the CPIES estimates are geostrophic. These upper-ocean fields, at times, have substantial curvature so that geostrophy would underestimate (overestimate) flow in anticyclonic (cyclonic) curvature (Holton 1979). The Rossby number defined as $\kappa V/f$, where $V$ is speed, provides an estimate of the difference between the gradient and geostrophic velocity. For example, the strong westward velocity peak at K2 near day 240 (Fig. 24) results from the passage of a warm-core eddy. Curvature was estimated from the 200-m dynamic height field, as in Watts et al. (1995). For this eddy, the Rossby number was near 0.3; thus, geostrophy underestimates gradient wind by 30%. A possible curvature correction to these fields has been left for a later time. In addition, we have not accounted for ADCP measurement errors ($<2$ cm $s^{-1}$) or possible velocity discrepancies resulting from uncertainty in MMP position (2–5 cm $s^{-1}$). Nevertheless, if the estimated error represents one standard deviation, then the rms differences are less than or equal at the five central and southern moorings and within 1.7 standard deviation at mooring K2. Note that uncertainty in ADCP pressure could also account for discrepancies. For example, at K7 the measured meridional velocities are weak compared to mapped estimates for most of the second-year deployment.

## 6. Conclusions

As part of the KESS process study, the first large-scale CPIES array was deployed. The goal of this paper was to

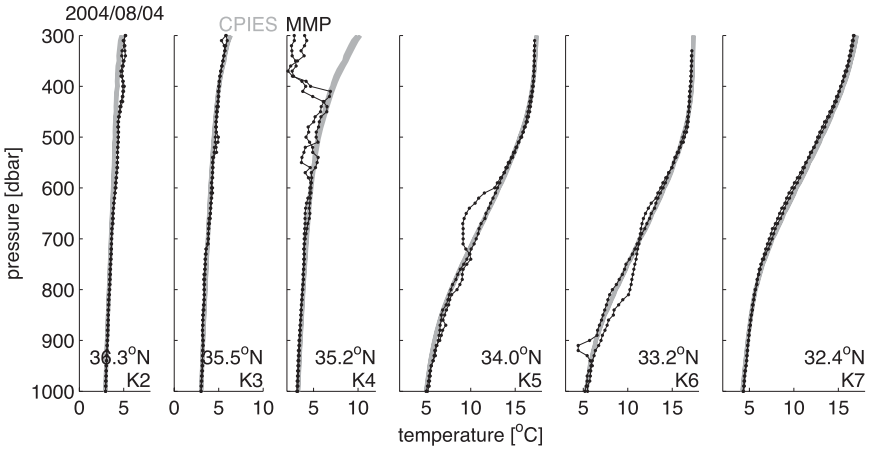


FIG. 22. Example of CPIES estimated profiles (gray lines) and MMP measured (black lines) profiles of temperature for 4 Aug 2004 across the breadth of the MMP moorings (left)–(right) from north to south; mooring indicated by text in bottom-right corner of each plots.

fully describe the methodology that led to maps of the mesoscale circulation in the KE. In doing so, this paper consolidates and documents the many advances that have taken place since an inverted echo sounder was tested off Bermuda (Rossby 1969) in their specific application to the KESS array: (i) the recognition that round-trip travel time can be used as a proxy for temperature and specific-volume anomaly profiles in strong-jet regimes via a GEM lookup table (Meinen and Watts 2000; Watts et al. 2001b); (ii) the methods to calibrate round-trip travel time compatible with the GEM (Meinen and Watts 1998) and the conversion to dynamic $\tau$ (Baker-Yeboah 2008); (iii) the inclusion of a seasonal cycle in the GEM lookup (Watts et al. 2001b); and (iv) appropriate multivariate and iterative optimal interpolation mapping techniques (Tracey et al. 1997; Watts et al. 2001a) for regimes with high mesoscale variability. The great depth of the Pacific and the large number of instruments presented new challenges that ultimately led to improved techniques to simultaneously dedrift and level the pressure data and determine error estimates.

Future researchers using CPIES data will benefit from having these collected advances in methodology consolidated. Research with the KESS array will aim to understand the processes coupling the upper and deep circulation and variability, to determine and quantify cross-frontal exchange processes in the KE, and to determine the processes that govern the strength and structure of the recirculation gyre. An initial look reveals a phenomenologically rich circulation field: steep troughs develop, rings form and interact with the KE, externally generated deep eddies arrive from the northeast, and deep eddies intensify locally under KE meanders. Specific present studies include a view of the KE structure in stream coordinates (Howe et al. 2009) and cyclogenesis of deep eddies via the interaction of deep Rossby waves with seamounts (Greene et al. 2009).

*Acknowledgments.* We gratefully acknowledge the efforts of the captains and crews of the R/V *Thompson*, R/V *Revelle*, and R/V *Melville*. The successful deployment and recovery of the CPIES was due to the instrument development and careful preparation by G. Chaplin and E. Sousa with the assistance of Gary Savoy

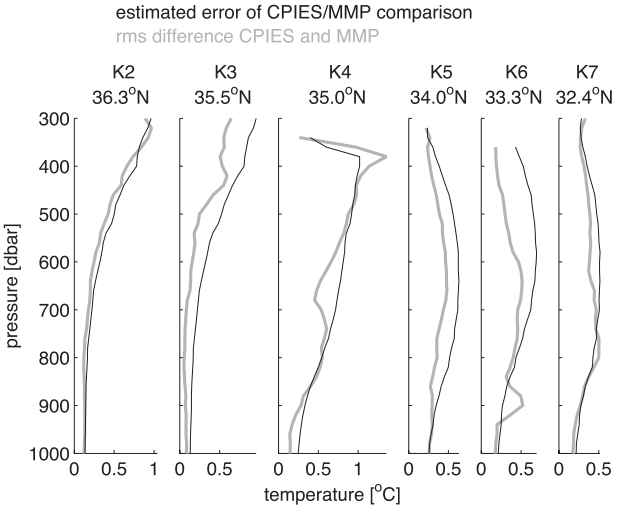


FIG. 23. The rms difference between MMP temperature measurement and CPIES mapped temperature estimate as a function of pressure and moored profiler (gray line). The MMP site is indicated in the title of each plot. The black line is the estimated error.

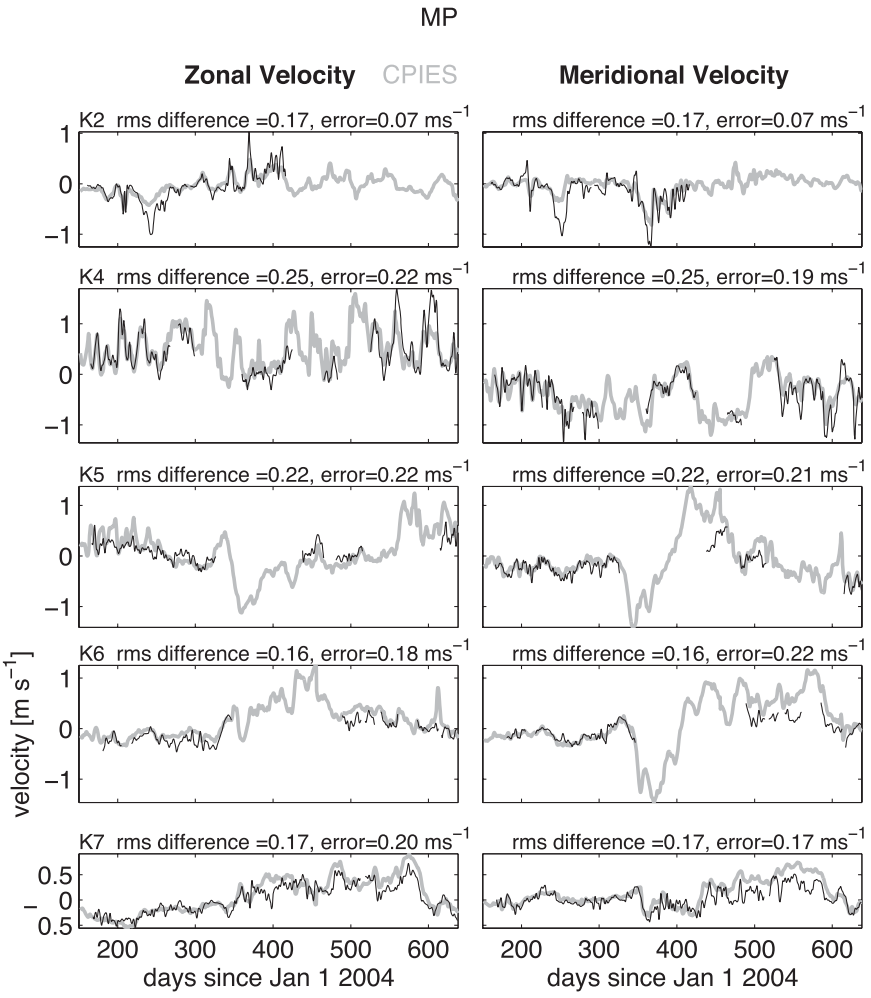


FIG. 24. Comparison between tall mooring ADCP velocity (black lines) at 200 dbar and CPIES estimate (gray lines) for both (left) zonal and (right) meridional velocity components across the MMP array. Tall mooring site is given at the top along with the rms difference between the two time series and the estimated optimal interpolation error estimate expressed as 1 std dev.

and Cathy Cipolla at the URI Equipment Development Laboratory. We appreciate the additional KESS data supplied by our colleagues at Woods Hole Oceanographic Institution, N. Hogg, S. Jayne, and L. Rainville, and University of Hawaii, P. Hacker and B. Qiu. This work was supported by the National Science Foundation (OCE-0221008).

## REFERENCES

Andres, M., M. Wimbush, J.-H. Park, K.-I. Chang, B.-H. Lim, D. R. Watts, H. Ichikawa, and W. J. Teague, 2008: Observations of Kuroshio flow variations in the East China Sea. *J. Geophys. Res.,* **113,** C05013, doi:10.1029/2007JC004200.

Baker-Yeboah, S., 2008: Sea surface height variability and the structure of eddies in the South Atlantic Cape Basin. Ph.D. dissertation, University of Rhode Island, 308 pp.

Book, J. W., M. Wimbush, S. Imawaki, H. Ichikawa, H. Uchida, and H. Kinoshita, 2002: Kuroshio temporal and spatial variations south of Japan determined from inverted echo sounder measurements. *J. Geophys. Res.,* **107,** 3121, doi:10.1029/2001JC000795.

Bretherton, F., R. E. Davis, and C. B. Fandry, 1976: A technique for objective analysis and design of oceanographic experiments applied to MODE-73. *Deep-Sea Res.,* **23,** 559–582.

Donohue, K. A., P. Hamilton, K. Leaman, R. Leben, M. Prater, E. Waddell, and D. Watts, 2006: Exploratory study of deep-water currents in the Gulf of Mexico. Volume II: Technical report. U.S. Department of the Interior Mineral Management Service Tech. Rep., OCS Study MMS 2006-074, 430 pp.

——, and Coauthors, 2008: Program studies the Kuroshio Extension. *Eos, Trans. Amer. Geophys. Union,* **89,** doi:10.1029/2008EO170002.

Greene, A., G. Sutyrin, and D. R. Watts, 2009: Deep cyclogenesis by synoptic eddies interacting with a seamount. *J. Mar. Res.,* **67,** 305–322, doi:10.1357/002224009789954775.

He, Y., D. R. Watts, and K. L. Tracey, 1998: Determining geostrophic velocity shear profiles with inverted echo sounders. *J. Geophys. Res.,* **103** (C3), 5607–5622.

Hogg, N. G., and D. E. Frye, 2007: Performance of a new generation of acoustic current meters. *J. Phys. Oceanogr.,* **37,** 148–161.

Holton, J. R., 1979: *An Introduction to Dynamic Meteorology*. Academic Press, 391 pp.

Houston, M. H., and J. M. Paros, 1998: High accuracy pressure instrumentation for underwater applications. *Proc. Int. Symp. on Underwater Technology,* Tokyo, Japan, IEEE, 307–311.

Howe, P., K. A. Donohue, and D. R. Watts, 2009: Stream-coordinate structure and variability of the Kuroshio Extension. *Deep-Sea Res. I,* **56,** 1093–1116, doi:10.1016/j.dsr.2009.03.007.

Kennelly, M. A., K. L. Tracey, and D. R. Watts, 2007: Inverted echo sounder data processing manual. University of Rhode Island GSO Tech. Rep. 2007-02, 89 pp.

——, K. A. Donohue, A. Greene, K. L. Tracey, and D. R. Watts, 2008: Inverted echo sounder data report: Kuroshio Extension System Study (KESS), April 2004 to July 2006. University of Rhode Island GSO Tech. Rep. 2008-02, 79 pp.

Koblinsky, C. J., R. L. Bernstein, W. J. Schmitz, and P. P. Niiler, 1984: Estimates of the geostrophic stream function in the western North Pacific from XBT surveys. *J. Geophys. Res.,* **89,** 10 451–10 460.

MacDonald, A. M., T. Suga, and R. G. Curry, 2001: An isopycnally averaged North Pacific climatology. *J. Atmos. Oceanic Technol.,* **18,** 394–420.

Meinen, C. S., and D. R. Watts, 1998: Calibrating inverted echo sounders equipped with pressure sensors. *J. Atmos. Oceanic Technol.,* **15,** 1339–1345.

——, and ——, 2000: Vertical structure and transport on a transect across the North Atlantic Current near 42°N: Time series and mean. *J. Geophys. Res.,* **105,** 21 869–21 891.

——, D. S. Luther, and M. O. Baringer, 2009: Structure, transport and potential vorticity of the Gulf Stream at 68°W: Revisiting older data sets with new techniques. *Deep-Sea Res. I,* **56,** 41–60, doi:10.1016/j.dsr.2008.07.010.

Munk, W., and D. Cartwright, 1966: Tidal spectroscopy and prediction. *Philos. Trans. Roy. Soc. London,* **259,** 533–581.

Park, J.-H., D. R. Watts, K. L. Tracey, and D. A. Mitchell, 2005: A multi-index GEM technique and its application to the Japan/East Sea. *J. Atmos. Oceanic Technol.,* **22,** 1282–1293.

Qiu, B., S. Chen, and P. Hacker, 2007: Effect of mesoscale eddies on Subtropical Mode Water variability from the Kuroshio Extension System Study (KESS). *J. Phys. Oceanogr.,* **37,** 982–1000.

Rossby, H. R., 1969: On monitoring depth variations of the main thermocline acoustically. *J. Geophys. Res.,* **74,** 5542–5546.

Sun, C., and D. Watts, 2001: A circumpolar gravest empirical mode for the Southern Ocean hydrography. *J. Geophys. Res.,* **106,** 2833–2855.

Teague, W. J., M. J. Carron, and P. J. Hogan, 1990: A comparison between the Generalized Digital Environmental Model and Levitus climatologies. *J. Geophys. Res.,* **95,** 7167–7183.

Tracey, K. L., and D. R. Watts, 1986: On Gulf Steam meander characteristics near Cape Hatteras. *J. Geophys. Res.,* **91,** 7587–7602.

——, S. D. Howden, and D. R. Watts, 1997: IES calibration and mapping procedures. *J. Atmos. Oceanic Technol.,* **14,** 1483–1493.

Trivers, G., and M. Wimbush, 1994: Using acoustic travel time to determine dynamic height variations in the North Atlantic Ocean. *J. Atmos. Oceanic Technol.,* **11,** 1309–1316.

URI/GSO, cited 2009: Dynamics of ocean currents and fronts: Inverted echo sounders (IES/PIES/CPIES). University of Rhode Island Graduate School of Oceanography. [Available online at http://po.gso.uri.edu/dynamics/IES/index.html.]

Watts, D. R., and H. T. Rossby, 1977: Measuring dynamic heights with inverted echo sounders: Results from MODE. *J. Phys. Oceanogr.,* **7,** 345–358.

——, and W. E. Johns, 1982: Gulf Stream meanders: Observations on propagation and growth. *J. Geophys. Res.,* **87,** 9467–9476.

——, and H. Kontoyiannis, 1990: Deep-ocean bottom pressure measurement: Drift removal and performance. *J. Atmos. Oceanic Technol.,* **7,** 296–306.

——, K. L. Tracey, and A. I. Friedlander, 1987: Producing accurate maps of the Gulf Stream thermal front using objective analysis. *J. Geophys. Res.,* **94,** 8040–8052.

——, ——, J. M. Bane, and T. J. Shay, 1995: Gulf Stream path and thermocline structure near 74°W and 68°W. *J. Geophys. Res.,* **100,** 18 291–18 312.

——, X. Qian, and K. L. Tracey, 2001a: Mapping abyssal current and pressure fields under the meandering Gulf Stream. *J. Atmos. Oceanic Technol.,* **18,** 1052–1067.

——, C. Sun, and S. Rintoul, 2001b: Gravest empirical modes determined from hydrographic observations in the Subantarctic Front. *J. Phys. Oceanogr.,* **31,** 2186–2209.

Yoshikawa, Y., J. A. Church, H. Uchida, and N. J. White, 2004: Near bottom currents and their relation to the transport in the Kuroshio Extension. *Geophys. Res. Lett.,* **31,** L16309, doi:10.1029/2004GL020068.